

## Article

# A Novel SiC Trench MOSFET with Self-Aligned N-Type Ion Implantation Technique

Baozhu Wang <sup>1,2</sup> , Hongyi Xu <sup>1,2,\*</sup> , Na Ren <sup>2,3</sup> , Hengyu Wang <sup>3</sup>, Kai Huang <sup>1</sup> and Kuang Sheng <sup>2,3</sup>

<sup>1</sup> School of Micro-Nano Electronics, Zhejiang University, Hangzhou 310027, China; wzbz@zju.edu.cn (B.W.); huangk@zju.edu.cn (K.H.)

<sup>2</sup> ZJU-Hangzhou Global Scientific and Technological Innovation Center, Hangzhou 311200, China; ren\_na@zju.edu.cn (N.R.); shengk@zju.edu.cn (K.S.)

<sup>3</sup> College of Electrical Engineering, Zhejiang University, Hangzhou 310027, China; wanghengyu@zju.edu.cn

\* Correspondence: xuhongyi@zju.edu.cn

**Abstract:** We propose a novel silicon carbide (SiC) self-aligned N-type ion implanted trench MOSFET (NITMOS) device. The maximum electric field in the gate oxide could be effectively reduced to below 3 MV/cm with the introduction of the P-epi layer below the trench. The P-epi layer is partially counter-doped by a self-aligned N-type ion implantation process, resulting in a relatively low specific on-resistance ( $R_{on,sp}$ ). The lateral spacing between the trench sidewall and N-implanted region ( $W_{sp}$ ) plays a crucial role in determining the performance of the SiC NITMOS device, which is comprehensively studied through the numerical simulation. With the  $W_{sp}$  increasing, the SiC NITMOS device demonstrates a better short-circuit capability owing to the reduced saturation current. The gate-to-drain capacitance ( $C_{gd}$ ) and gate-to-drain charge ( $Q_{gd}$ ) are also investigated. It is observed that both  $C_{gd}$  and  $Q_{gd}$  decrease as the  $W_{sp}$  increases, owing to the enhanced screen effect. Compared to the SiC double-trench MOSFET device, the optimal SiC NITMOS device exhibits a 79% reduction in  $C_{gd}$ , a 38% decrease in  $Q_{gd}$ , and a 41% reduction in  $Q_{gd} \times R_{on,sp}$ . A higher switching speed and a lower switching loss can be achieved using the proposed structure.

**Keywords:** silicon carbide (SiC); trench MOSFET; self-aligned; P-epi layer; oxide protection



**Citation:** Wang, B.; Xu, H.; Ren, N.; Wang, H.; Huang, K.; Sheng, K. A Novel SiC Trench MOSFET with Self-Aligned N-Type Ion Implantation Technique. *Micromachines* **2023**, *14*, 2212. <https://doi.org/10.3390/mi14122212>

Academic Editor: Ling Li

Received: 31 October 2023

Revised: 11 November 2023

Accepted: 16 November 2023

Published: 7 December 2023



**Copyright:** © 2023 by the authors. Licensee MDPI, Basel, Switzerland. This article is an open access article distributed under the terms and conditions of the Creative Commons Attribution (CC BY) license (<https://creativecommons.org/licenses/by/4.0/>).

## 1. Introduction

Silicon carbide (SiC) power devices show great potential in high-voltage and high-temperature power electronics applications due to their superior material properties, such as a wide band gap, high critical electric field, high electron saturation velocity and high thermal conductivity [1,2]. SiC MOSFET devices can realize higher switching speeds and lower switching losses than the conventional Si power devices and have been widely applied in electric vehicles [3–5]. However, SiC planar MOSFET devices still have relatively high specific on-resistance ( $R_{on,sp}$ ) owing to their low channel mobility [6,7]. On the other hand, SiC trench MOSFET (TMOS) devices are expected to realize a lower  $R_{on,sp}$  owing to the absence of the JFET region, smaller cell pitch and higher channel mobility on the trench sidewall [8]. However, during the blocking state, SiC trench MOSFET devices suffer from a high electric field in the gate oxide at the trench corner, which can result in long-term reliability issues [9].

The P+ shield regions are commonly introduced in SiC trench MOSFET devices to alleviate the electric field crowding at the trench corner. In recent years, various structural enhancements have been implemented in SiC trench MOSFET devices to address the aforementioned issues, such as SiC double trench MOSFET (DTMOS) [10], SiC implantation-and-epitaxial trench MOSFET (IETMOS) [11], SiC asymmetrical cell trench MOSFET (ATMOS) [12], SiC trench MOSFET with multiple-ion-implantation into tilted trench side walls (MIT<sup>2</sup>-MOS) [13] and Fin-SiC TMOS [14]. The fabrication process of the SiC DTMOS device includes an extra step of etching the source trench, followed by a vertical self-aligned P-type

ion implantation to form the P+ shield region. In addition, a tilted P-type ion implantation into the sidewalls of the source trench is utilized to achieve a short connection between the P+ shield region and the source. The SiC IETMOS device requires two additional P-type ion implantations and two additional epi-layer regrowth steps to create the P+ shield region. In the SiC MIT<sup>2</sup>-MOS device, the P+ shield region can be simply formed through a vertical self-aligned P-type ion implantation into the bottom of the gate trench. However, an additional tilted Al implantation is required for grounding, which will reduce the current conducting area of the device. The P+ shield regions in the SiC ATMOS and Fin-SiC TMOS devices are formed only through ultra-high energy (MeV) ion implantation. However, this process results in the introduction of more defects that need to be repaired and makes it challenging to control the shape of the implanted region, which is crucial for device performance. Therefore, to simplify and improve the fabrication process, an easy-to-fabricate structure is required.

In this work, a novel self-aligned N-type ion implanted SiC trench MOSFET (NITMOS) device is proposed and studied. The device features P-type regions located below the trench, partially overlapping with both sides of the trench bottom in the vertical direction. The presence of these P-type regions introduces an undesirable JFET region, which can be optimized to achieve a low  $R_{on,sp}$  and maximum electric field in the gate oxide at the same time. In addition, the short circuit capability and gate-to-drain capacitance are investigated using numerical simulations.

## 2. Device Structure and Parameters

Figure 1 shows the schematic cross sections of SiC NITMOS and SiC DTMOS devices. A P-type epitaxial layer (P-epi in Figure 1a) grown on top of the N drift layer was utilized to protect the gate oxide at the trench bottom. The proposed SiC NITMOS device was based on the self-aligned N-type implantation technology to incorporate N-type regions (N-imp in Figure 1a), and conduct currents through the P-epi layer. The lateral spacing between the trench sidewall and N-imp ( $W_{sp}$  in Figure 1a) can be precisely controlled through a self-alignment process. A relatively heavy doping current spreading layer (CSL in Figure 1a) was introduced to decrease the depletion width caused by the P-epi layer and expand the current conducting region. The P+ region was utilized to achieve a short connection between the P-epi layer and the source. Compared to the floating P-type shield region, the grounded P-type shield region can effectively reduce the maximum electric field in the gate oxide, increase the switching speed of the device and improve the short-circuit capability of the device, which contributes to enhancing the device performance and reliability [15–17]. Considering the current fabrication capabilities, the trench width (TW in Figure 1a), trench depth (TD in Figure 1a), and cell pitch of the device were set to 1  $\mu\text{m}$ , 1  $\mu\text{m}$  and 3  $\mu\text{m}$ , respectively. The channel had a length of 0.4  $\mu\text{m}$  and an electron mobility of 40  $\text{cm}^2/\text{V}\cdot\text{s}$  [18,19]. Furthermore, the thickness of the gate oxide was 50 nm at the sidewall and bottom of the trench. The simulation parameters are summarized in Table 1.

**Table 1.** Device parameters used in simulation.

Parameters	Value	Unit
N+ doping	$1.0 \times 10^{19}$	$\text{cm}^{-3}$
N+ thickness	0.3	$\mu\text{m}$
P+ doping	$2.0 \times 10^{18}$	$\text{cm}^{-3}$
P-well doping	$1.5 \times 10^{17}$	$\text{cm}^{-3}$
P-well thickness	0.4	$\mu\text{m}$
CSL doping	$5.0 \times 10^{16}$	$\text{cm}^{-3}$
CSL thickness	0.6	$\mu\text{m}$

Table 1. Cont.

Parameters	Value	Unit
P-epi doping	$6.0 \times 10^{17}$	$\text{cm}^{-3}$
P-epi thickness	0.5	$\mu\text{m}$
N-imp doping	$1.0 \times 10^{17}$	$\text{cm}^{-3}$
Trench width (TW)	1.0	$\mu\text{m}$
Trench depth (TD)	1.0	$\mu\text{m}$
Lateral spacing between trench sidewall and N-imp ( $W_{sp}$ )	0–0.4	$\mu\text{m}$

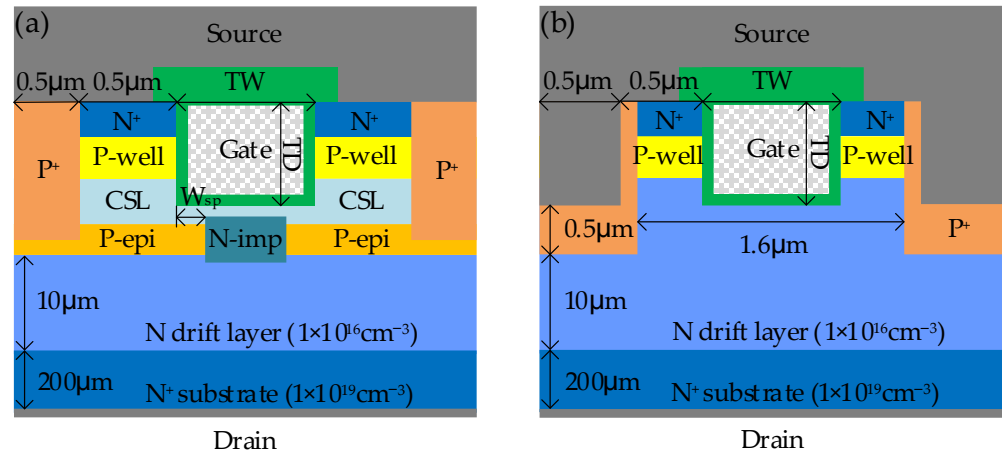


Figure 1. Schematic cross sections and key parameters of (a) SiC NITMOS and (b) SiC DTMOS cell structures.

In this work, Silvaco was utilized to conduct both device and mixed-mode simulations. In the simulation, the electron/hole continuity and Poisson equations were solved self-consistently, considering the Shockley–Read–Hall recombination, carrier generation, complete dopant ionization, electron/hole mobility, electron/hole saturation velocity, and impact ionization. The key physical models are specified below:

(1) The mobility model utilized in our analysis takes into consideration the impact of doping concentration, electric field, and temperature on the carrier mobility. This model accurately represents the behavior of carrier transport within the device. The low field mobilities, which are dependent on doping concentration and temperature, can be described using the following analytical function, based on the work by Caughey and Thomas [20]:

$$\mu_{n0,p0} = \mu_{n,p}^{\min} \left( \frac{T}{300 \text{ K}} \right)^{\alpha_{n,p}} + \frac{\mu_{n,p}^{\max} \left( \frac{T}{300 \text{ K}} \right)^{\beta_{n,p}} - \mu_{n,p}^{\min} \left( \frac{T}{300 \text{ K}} \right)^{\alpha_{n,p}}}{1 + \left( \frac{T}{300 \text{ K}} \right)^{\gamma_{n,p}} \left( \frac{N}{N_{n,p}^{\text{crit}}} \right)^{\delta_{n,p}}}$$

where  $N$  is the local impurity concentration in  $\text{cm}^{-3}$  and  $T$  is the temperature in degrees Kelvin.  $N_n^{\text{crit}} = 1.94 \times 10^{17} \text{ cm}^{-3}$  and  $N_p^{\text{crit}} = 1.76 \times 10^{19} \text{ cm}^{-3}$ . While  $\mu_n^{\min} = 0 \text{ cm}^2/\text{V}\cdot\text{s}$ ,  $\mu_p^{\min} = 15.9 \text{ cm}^2/\text{V}\cdot\text{s}$ ,  $\mu_n^{\max} = 947 \text{ cm}^2/\text{V}\cdot\text{s}$  and  $\mu_p^{\max} = 124 \text{ cm}^2/\text{V}\cdot\text{s}$ . In addition, the coefficients  $\alpha_{n,p}$ ,  $\beta_{n,p}$ ,  $\gamma_{n,p}$ , and  $\delta_{n,p}$  are fitting coefficients used in the model.

(2) The saturation effect on carrier drift velocity under high electric fields is taken into account, which accurately accounts for the limitation of carrier velocity in the device and its influence on overall device performance. As carriers are accelerated in an electric field, their velocity will saturate when the electric field magnitude reaches a significant level. The field-dependent mobility is implemented using the following Caughey and Thomas Expression [20]. This expression provides a smooth transition between low-field

and high-field behavior, effectively describing the carrier behavior under various electric field conditions.

$$\mu_{n,p}(E) = \frac{\mu_{n0,p0}}{\left(1 + \left(\frac{\mu_{n0,p0}E}{v_{sat}}\right)^{\beta_E}\right)^{\frac{1}{\beta_E}}}$$

where  $E$  is the parallel electric field,  $\beta_E$  is the fitting coefficient, and  $\mu_{n0}$  and  $\mu_{p0}$  are the low field electron and hole mobilities, respectively. In addition, the saturation velocity ( $v_{sat}$ ) is approximately  $2.0 \times 10^7$  cm/s for both electrons and holes.

(3) The impact ionization model used in the simulation was proposed by S. Selberherr [21], which is based on the following equation:

$$\alpha_{n,p}(E) = A_{n,p} \exp\left[-\left(\frac{B_{n,p}}{E}\right)^{\beta_{n,p}}\right]$$

where  $A_{n,p}$ ,  $B_{n,p}$  and  $\beta_{n,p}$  are fitting coefficients. The values of these parameters were selected by fitting experimental results presented by A. O. Konstantinov [22]. The impact ionization coefficients  $\alpha_n$  and  $\alpha_p$  as a function of electric field  $E$  can be expressed as

$$\alpha_n(E) = 7.26 \times 10^6 \cdot \exp\left[-\frac{2.34 \times 10^7}{E}\right] \text{cm}^{-1}$$

$$\alpha_p(E) = 7.26 \times 10^6 \cdot \exp\left[-\frac{2.34 \times 10^7}{E}\right] \text{cm}^{-1}$$

These simulation models and parameters utilized in this work have also been applied in other research conducted by our group, which includes various devices such as SiC junction barrier Schottky diodes (JBS), SiC trench junction barrier Schottky diodes (TJBS), SiC planar MOSFET devices, SiC Super Junction Schottky diodes (SJ SBD) and SiC Super Junction JFET devices (SJ JFET) [23–26]. The simulated results of those devices are in good agreement with the experimental results obtained from fabricated devices.

### 3. Device Simulation and Results Discussion

The  $W_{sp}$  is of great significance to the SiC NITMOS device performance. Considering the trench width of 1  $\mu\text{m}$ , the SiC NITMOS devices with a  $W_{sp}$  varying from 0  $\mu\text{m}$  to 0.4  $\mu\text{m}$  were studied. The simulated output and blocking characteristics of SiC DTMOS and SiC NITMOS devices with varying  $W_{sp}$  are shown in Figure 2. These results show that with the  $W_{sp}$  increasing from 0  $\mu\text{m}$  to 0.4  $\mu\text{m}$ , the SiC NITMOS device exhibited a progressive degradation in current conduction capability and reached a nearly non-conductive state at  $W_{sp} = 0.4 \mu\text{m}$ . The SiC DTMOS device showed a comparable conducting current to that of the SiC NITMOS device, with  $W_{sp} = 0.2 \mu\text{m}$ .

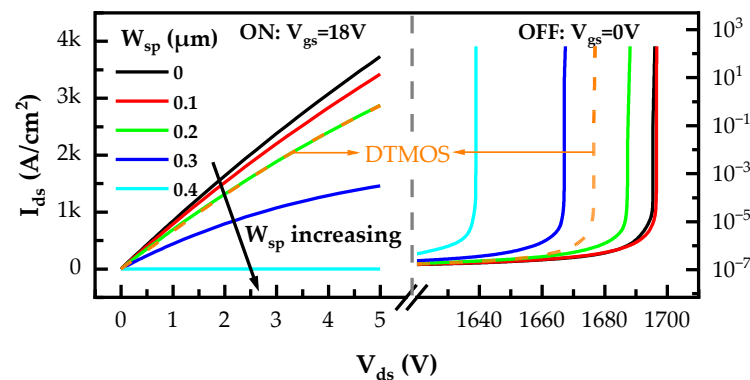


**Figure 2.** Simulated output and blocking characteristics of SiC DTMOS and SiC NITMOS devices with varying  $W_{sp}$ .

The specific on-resistances ( $R_{on,sp}$ ), breakdown voltages (BV) and maximum electric fields in the gate oxide ( $E_{ox,max}$ ) of the SiC NITMOS devices with varying  $W_{sp}$  are plotted in Figure 3. The  $R_{on,sp}$  of these simulated structures were extracted at  $V_{ds} = 1$  V and the breakdown voltages were extracted at a leakage current density of  $10^{-3}$  A/cm<sup>2</sup> from their  $I_{ds}-V_{ds}$  characteristics, where the avalanche breakdown in the device had already occurred. When the  $W_{sp}$  increased from 0  $\mu\text{m}$  to 0.3  $\mu\text{m}$ , the  $R_{on,sp}$  of the SiC NITMOS devices increased from 1.59  $\text{m}\Omega\cdot\text{cm}^2$  to 2.69  $\text{m}\Omega\cdot\text{cm}^2$ . When the  $W_{sp}$  exceeded 0.3  $\mu\text{m}$ , the device exhibited a sharp and substantial increase in the specific on-resistance. Such increments are attributed to the reduction in the width of the JFET region (the region inside the white dashed box in Figure 4) with the increasing  $W_{sp}$ , as shown in Figure 4. As the  $W_{sp}$  increased, the BV initially increased slightly and then decreased, reaching its maximum value of 1696 V at  $W_{sp} = 0.1$   $\mu\text{m}$ . The  $E_{ox,max}$  was obtained at a blocking voltage of 1200 V and demonstrated a linear decrease with increasing  $W_{sp}$ . The impact of the  $W_{sp}$  on the  $E_{ox,max}$  was explored using the electric field analysis, as shown in Figures 5 and 6.

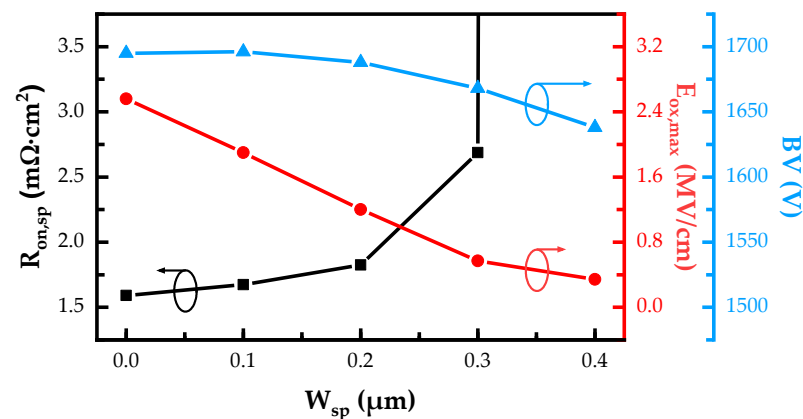


Figure 3. Simulated  $R_{on,sp}$ ,  $E_{ox,max}$  and BV of the SiC NITMOS devices with varying  $W_{sp}$ .

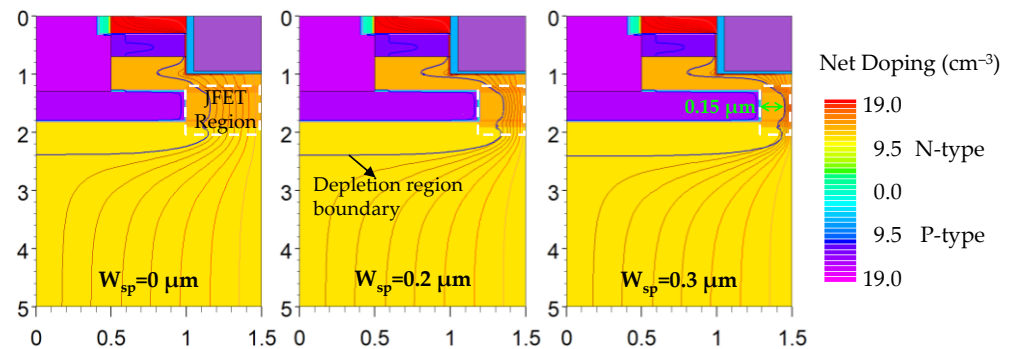
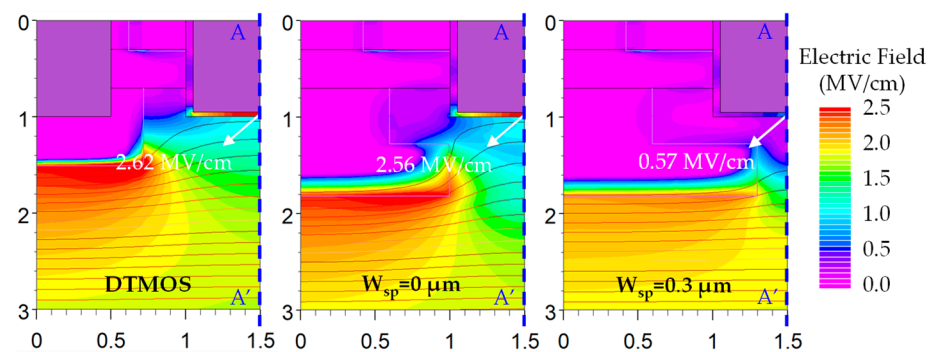


Figure 4. Simulated depletion region boundary and current flowline distributions of the SiC NITMOS devices with  $W_{sp} = 0, 0.2$  and  $0.3$   $\mu\text{m}$  at  $V_{gs} = 18$  V and  $V_{ds} = 1$  V.

The simulated depletion region boundary and current flowline distributions of the SiC NITMOS devices with  $W_{sp} = 0, 0.2$  and  $0.3$   $\mu\text{m}$  at a gate-source voltage of 18 V and a drain-source voltage of 1 V are displayed in Figure 4. As the  $W_{sp}$  increased, the width of the JFET region decreased, resulting in increased crowding of the conducting current and an increase in the specific on-resistance. This effect was particularly pronounced when the  $W_{sp}$  increased from 0.2  $\mu\text{m}$  to 0.3  $\mu\text{m}$ , as shown in Figure 3. The maximum depletion width in the N-imp region induced by the P-epi layer was 0.15  $\mu\text{m}$ . This implies that when the  $W_{sp}$  exceeds 0.35  $\mu\text{m}$ , the adjacent depletions will merge, resulting in a loss of the device’s current conducting capability.

In order to ensure the long-term reliability of the device, it is generally recommended to maintain the  $E_{ox,max}$  below 3 MV/cm [27–29]. The simulated electric field and equal

potential line distributions of SiC DTMOS and SiC NITMOS devices with  $W_{sp} = 0 \mu\text{m}$  and  $0.3 \mu\text{m}$  at a gate-source voltage of  $0 \text{ V}$  and a drain-source voltage of  $1200 \text{ V}$  are depicted in Figure 5. It can be observed that the  $E_{ox,max}$  of SiC DTMOS and SiC NITMOS devices are located at the middle of the trench bottom, rather than at the corner of the trench bottom [10]. The  $E_{ox,max}$  of the SiC NITMOS device is much lower than  $3 \text{ MV/cm}$ . With the presence of the P-epi layer, the potential lines are prevented from passing through the N-imp region, mitigating the electric field crowding at the trench bottom. By increasing the  $W_{sp}$  from  $0 \mu\text{m}$  to  $0.3 \mu\text{m}$ , a significant reduction in the  $E_{ox,max}$  is observed, decreasing from  $2.56 \text{ MV/cm}$  to  $0.57 \text{ MV/cm}$ . Such a reduction ensures the good long-term reliability of the gate oxide [30]. The  $E_{ox,max}$  of the SiC DTMOS device was  $2.62 \text{ MV/cm}$ , which was slightly higher than that of the SiC NITMOS device with  $W_{sp} = 0 \mu\text{m}$ . Figure 6 shows the electric field distributions along A–A' of the SiC DTMOS and SiC NITMOS devices with varying  $W_{sp}$  in Figure 5. With the  $W_{sp}$  increasing from  $0 \mu\text{m}$  to  $0.4 \mu\text{m}$ , the electric field at  $y = 2.4 \mu\text{m}$  experienced an increase, while the electric field at  $y = 1.3 \mu\text{m}$  and near the trench bottom was gradually reduced to  $0 \text{ MV/cm}$ . In addition, in the region between  $y = 3 \mu\text{m}$  and  $y = 12 \mu\text{m}$ , the electric field of the SiC DTMOS device was slightly lower than that of the SiC NITMOS device. However, near the trench bottom, the electric field of the SiC DTMOS device was significantly higher compared to the SiC NITMOS device, as shown in the inset of Figure 6. Such an observation indicates that the SiC NITMOS device shows a more effective shielding effect. This shielding effect in the SiC NITMOS device, induced by the P-epi layer, exhibits a comparable ability to reduce the electric field near the trench bottom. This effect can significantly mitigate electric field crowding, resulting in an improved device performance and reliability.



**Figure 5.** Simulated electric field and equal potential line distributions of SiC DTMOS and SiC NITMOS devices with  $W_{sp} = 0 \mu\text{m}$  and  $0.3 \mu\text{m}$  at  $V_{gs} = 0 \text{ V}$  and  $V_{ds} = 1200 \text{ V}$ . The step of equal potential lines is  $20 \text{ V}$ .

In addition, the short-circuit capabilities of the SiC DTMOS and SiC NITMOS devices were estimated using the test circuit illustrated in Figure 7a. The DC voltage ( $V_{DC}$ ) was  $800 \text{ V}$  and the pulse width, i.e., the short circuit duration time ( $t_{SC}$ ), was  $5 \mu\text{s}$ . The simulated short-circuit test waveforms of the SiC DTMOS and SiC NITMOS devices with varying  $W_{sp}$  are presented in Figure 7b. With the  $W_{sp}$  increasing from  $0 \mu\text{m}$  to  $0.3 \mu\text{m}$ , the maximum short-circuit current density ( $I_{SC,max}$ ) of the SiC NITMOS devices decreased from  $4540 \text{ A/cm}^2$  to  $2404 \text{ A/cm}^2$ . This decrease is attributed to the reduced saturation current, as shown in Figure 2. The  $I_{SC,max}$  of the SiC DTMOS device was  $3781 \text{ A/cm}^2$ , which was slightly higher than that of the SiC NITMOS with  $W_{sp} = 0.2 \mu\text{m}$ . The energy dissipations of the SiC DTMOS and SiC NITMOS devices with varying  $W_{sp}$  in the short circuit tests were also calculated, as shown in Figure 7c. As the  $W_{sp}$  increased from  $0 \mu\text{m}$  to  $0.3 \mu\text{m}$ , the generated energy density of the SiC NITMOS device decreased from  $14.92 \text{ J/cm}^2$  to  $8.82 \text{ J/cm}^2$ . The lower energy density in the SiC NITMOS device resulted in reduced heat dissipation during the short-circuit period. This reduction indicates that the SiC NITMOS device with a larger  $W_{sp}$  possesses a better short-circuit capability and a longer short-circuit withstand time [31–33].

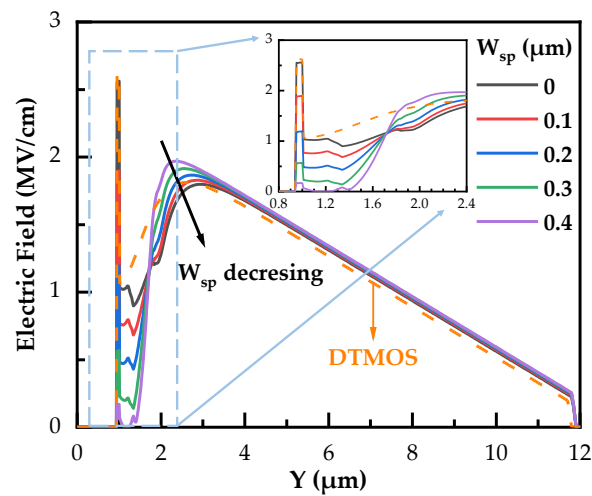


**Figure 6.** Simulated electric field distributions along A–A’ of SiC DTMOS and SiC NITMOS devices with varying  $W_{sp}$ .

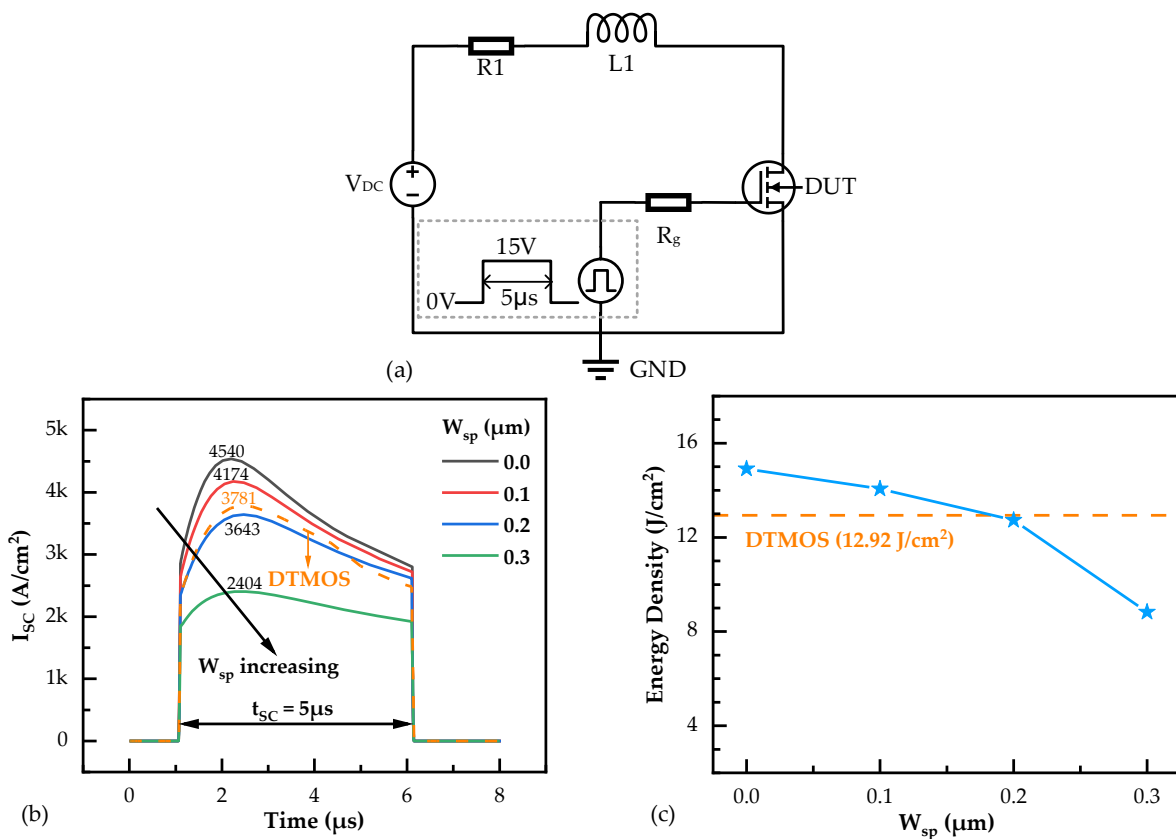


**Figure 7.** (a) The test circuit for the short circuit used in the simulation. (b) Drain current densities of SiC DTMOS and SiC NITMOS devices with varying  $W_{sp}$  under the short-circuit conditions at a DC voltage of 800 V. (c) Energy dissipations of SiC DTMOS and SiC NITMOS devices with varying  $W_{sp}$  in the short circuits at a DC voltage of 800 V.

The  $W_{sp}$  also plays a critical role in influencing the gate-to-drain capacitance ( $C_{gd}$ ) of the SiC NITMOS devices, which has a significant impact on the switching performance [34–36]. The  $C_{gd}$  values of SiC DTMOS and SiC NITMOS devices with varying  $W_{sp}$  are plotted in Figure 8. The SiC DTMOS device exhibited the highest  $C_{gd}$  during high-drain-source voltage conditions compared to the SiC NITMOS devices. This is because the

gate was completely exposed to the drain in the SiC DTMOS device. The SiC NITMOS device exhibited a reduced  $C_{gd}$  as the  $W_{sp}$  increased. This is due to the enhanced screen effect, which reduced the coupling between the gate and drain, resulting in a lower  $C_{gd}$ . The gate charges of the studied devices were evaluated using the test circuit shown in Figure 9a. The DC voltage was 800 V and an ideal diode was used as the freewheeling diode. As can be seen from Figure 9b, the  $Q_{gd}$  of the SiC DTMOS device was  $323 \text{ nC/cm}^2$ , which was slightly lower than that of the SiC NITMOS device with  $W_{sp} = 0 \text{ }\mu\text{m}$ . This can be attributed to the fact that the SiC DTMOS device had lower  $C_{gd}$  in the range of  $V_{ds} < 15 \text{ V}$ . For the SiC NITMOS devices, as the  $W_{sp}$  increased from  $0 \text{ }\mu\text{m}$  to  $0.3 \text{ }\mu\text{m}$ , the  $Q_{gd}$  decreased from  $361 \text{ nC/cm}^2$  to  $123 \text{ nC/cm}^2$ , which is significantly lower than that in the SiC DTMOS device.

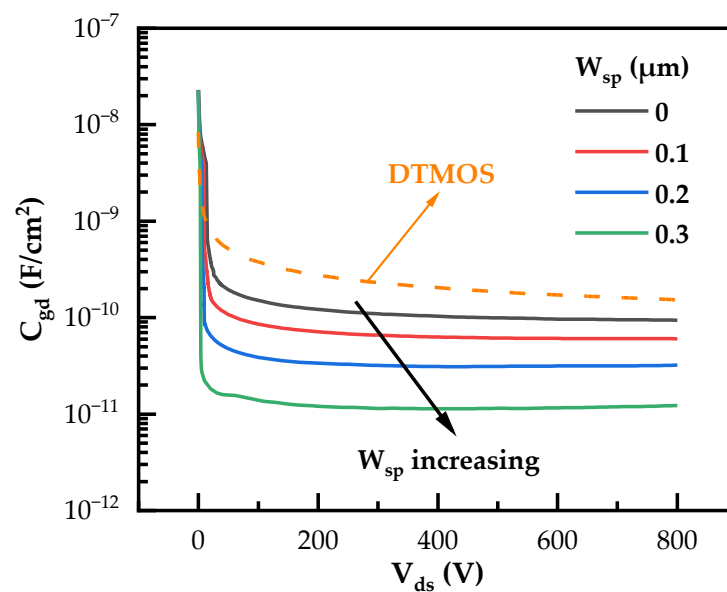


Figure 8.  $C_{gd}$ - $V_{ds}$  curves of SiC DTMOS and SiC NITMOS devices with varying  $W_{sp}$ .

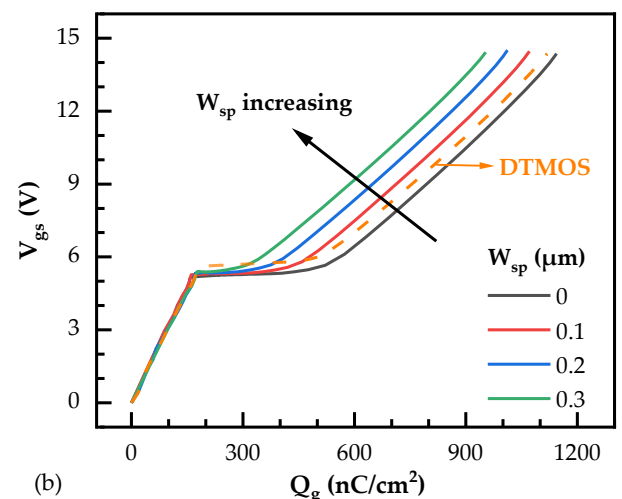
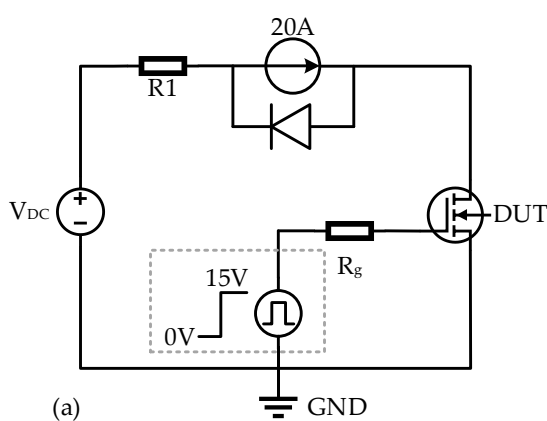


Figure 9. (a) The test circuit for the gate charges used in the simulation. The DC voltage was 800 V during the test. (b) Gate charges versus gate-source voltage for SiC DTMOS and SiC NITMOS devices with varying  $W_{sp}$ .

The key characteristics of the SiC DTMOS and SiC NITMOS devices are summarized in Table 2 for comparison. Among the SiC NITMOS devices, the device with  $W_{sp} = 0 \mu\text{m}$  demonstrated a superior Baliga's Figure of Merit (BFOM). However, the device also had the highest values for  $E_{ox,max}$ ,  $C_{gd}$  and  $Q_{gd} \times R_{on,sp}$ . On the other hand, the devices with  $W_{sp} = 0.2 \mu\text{m}$  and  $0.3 \mu\text{m}$  demonstrated lower  $E_{ox,max}$ , and similar  $Q_{gd} \times R_{on,sp}$ . In addition, the device with  $W_{sp} = 0.2 \mu\text{m}$  exhibited a better BFOM. Taking all factors into consideration, the device with  $W_{sp} = 0.2 \mu\text{m}$  seems to have the best structure. Compared to the SiC DTMOS device, the SiC NITMOS device with  $W_{sp} = 0.2 \mu\text{m}$  showed significant improvements, with a 79% reduction in  $C_{gd}$ , a 38% decrease in  $Q_{gd}$ , and a 41% reduction in  $Q_{gd} \times R_{on,sp}$ . Such significant reductions can result in higher switching speeds and lower switching losses.

**Table 2.** Summarized device performance.

	DTMOS	NITMOS ( $W_{sp}/\mu\text{m}$ )				Unit
		0	0.1	0.2	0.3	
$R_{on,sp}$	1.92	1.59	1.67	1.82	2.69	$\text{m}\Omega \cdot \text{cm}^2$
BV	1676	1694	1696	1688	1668	V
$E_{ox,max}$	2.62	2.56	1.90	1.20	0.57	$\text{MV}/\text{cm}$
BFOM <sup>a</sup>	1.46	1.81	1.72	1.56	1.03	$\text{GW}/\text{cm}^2$
$C_{gd}$ <sup>b</sup>	153	94	60	32	12	$\text{pF}/\text{cm}^2$
$Q_{gd}$	323	361	282	201	123	$\text{nC}/\text{cm}^2$
$Q_{gd} \times R_{on,sp}$	620	574	471	366	331	$\text{m}\Omega \cdot \text{nC}$

<sup>a</sup> BFOM is the value of  $\text{BV}^2/R_{on,sp}$ . <sup>b</sup> The  $C_{gd}$  is extracted at  $V_{ds} = 800 \text{ V}$ .

#### 4. Device Fabrication Process

A simple and practical fabrication process for the SiC NITMOS device is provided in Figure 10. The fabrication process begins with an N+ substrate and three epitaxial layers, including the N drift, P-epi and CSL layers (Figure 10a). The P-well and N+ regions are sequentially formed by a series of ion implantation steps (Figure 10b). The P+ region is implanted deeply into the P-epi layer to establish a short connection between the P-epi layer and the source (Figure 10c). The gate trench is etched using an Inductively Coupled Plasma (ICP) etching system with a  $\text{SiO}_2$  mask (Figure 10d). Subsequently, a  $\text{SiO}_2$  layer is deposited without removing the etch mask, and followed by an overall etchback process. The remaining  $\text{SiO}_2$  sidewall serves as a mask for self-aligned N-type ion implantation to create the N-imp region (Figure 10e), which is a critical process in the overall fabrication of the SiC NITMOS device. This process is of utmost importance, because it plays a vital role in determining the value of  $W_{sp}$ . Following the formation of the N-imp region, the gate oxide layer is grown. Subsequently, polysilicon is deposited and precisely etched back to form the gate electrode (Figure 10f). After gate electrode formation, the deposited interlayer dielectric (ILD) layer undergoes an etching and patterning process to expose the source region (Figure 10g). Finally, the source and drain electrodes are formed to complete device fabrication (Figure 10h).

Table 3 presents a comparative analysis of the key fabrication processes among different SiC TMOS devices, specifically focusing on the formation of the P-type shield region and its short connection to the source. Compared to the SiC DTMOS, SiC IETMOS and SiC MIT<sup>2</sup>-MOS devices, the SiC NITMOS device requires fewer fabrication steps. In addition to the SiC NITMOS device, the SiC ATMOS and Fin-SiC TMOS devices also require fewer fabrication steps. However, these devices involve the P-type ion implantation with ultra-high energy (MeV), which presents challenges in controlling the shape of the P+ shield region. The shape of the P+ shield region plays a crucial role in device performance and requires careful attention during the device fabrication.

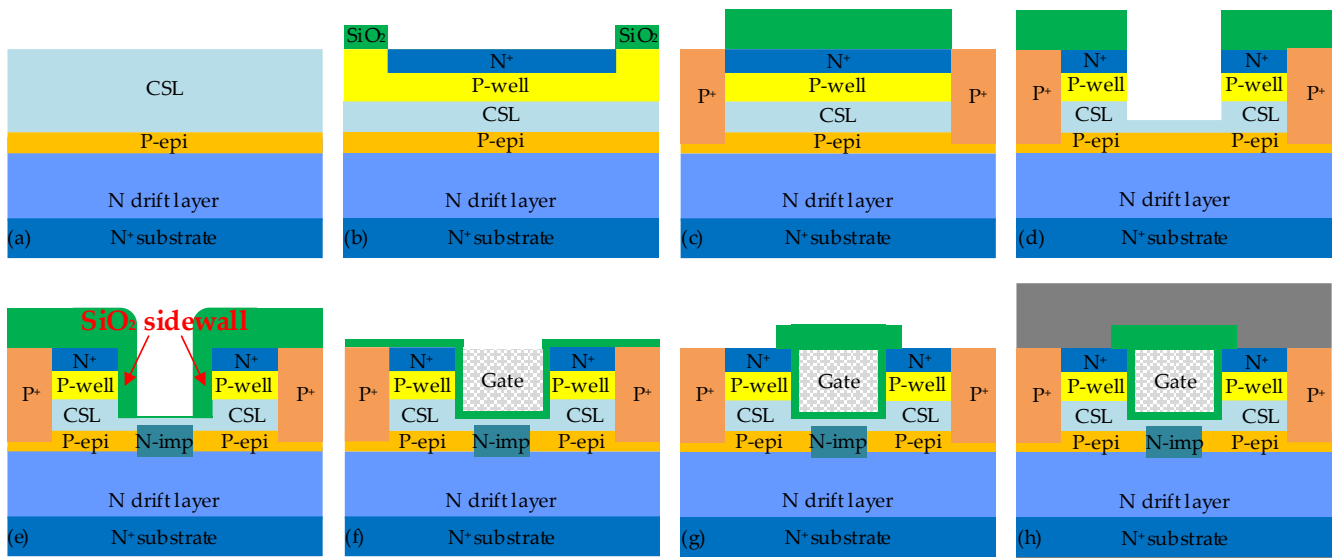


**Figure 10.** The proposed fabrication process for the SiC NITMOS device. (a) Starting wafer (b) P-well and N+ implantation (c) P+ implantation (d) Trench etching (e) N-imp implantation (f) Gate formation (g) Source region opening (h) Source and Drain electrodes formation.

**Table 3.** Key fabrication processes of various SiC TMOS devices.

Device	Formation of the P-Type Shield Region	Shorted to the Source (Grounding)
SiC NITMOS	1. The P-epi layer partially counter-doped by a self-aligned N-type ion implantation	—
SiC DTMOS [10]	1. The etching of the source trench 2. The vertical self-aligned P-type ion implantation into the bottom of the source trench	The titled P-type ion implantation into the sidewalls of the source trench
SiC IETMOS [11]	1. 1st P-type ion implantation in the N-type drift to form 1st P+ shield region 2. Followed by an N-type epi-layer regrowth 3. 2nd P-type ion implantation in the N-type epi-layer to form 2nd P+ shield region 4. A P-type epi-layer regrowth used as the P-well	—
SiC ATMOS [12]	1. The ultra-high energy P-type ion implantation	—
SiC MIT <sup>2</sup> -MOS [13]	1. The vertical self-aligned P-type ion implantation into the bottom of the gate trench	The tilted P-type ion implantation into the one side of the gate trench sidewall
Fin-SiC TMOS [14]	1. The ultra-high energy P-type ion implantation	—

“—” indicates no additional steps are needed to achieve the short connection to the source.

### 5. Conclusions

In this work, a SiC TMOS device with a self-aligned N-type ion implantation technique was proposed. The impact of the  $W_{sp}$  on the device performance was comprehensively studied by numerical simulations. The presence of the P-epi layer effectively reduced the maximum electric field in the gate oxide, and the N-imp region enabled a relatively low specific on-resistance. Furthermore, the SiC NITMOS device demonstrated an improved short-circuit capability owing to the optimization of the JFET region. The gate-to-drain capacitance ( $C_{gd}$ ) and gate-to-drain charge ( $Q_{gd}$ ) of the SiC NITMOS device were significantly lower compared to the SiC DTMOS device. Such reductions are attributed to the effective screening of the coupling between the gate and drain by the P-epi layer. The superior device performance and simplicity of the manufacturing process make the proposed SiC NITMOS device highly suitable for mass production and commercialization.

**Author Contributions:** Conceptualization, B.W. and H.X.; methodology, K.S. and K.H.; software, B.W.; validation, B.W., H.X. and N.R.; formal analysis, B.W.; investigation, H.X.; resources, N.R.; data curation, H.X.; writing—original draft preparation, B.W.; writing—review and editing, H.X. and H.W.; funding acquisition, N.R. and K.S. All authors have read and agreed to the published version of the manuscript.

**Funding:** This research was supported by Science and Technology Program of Zhejiang Province, grant number 2022C01235. The APC was funded by ZJU-Hangzhou Global Scientific and Technological Innovation Center, Hangzhou 311200, China.

**Data Availability Statement:** Data are contained within the article.

**Conflicts of Interest:** The authors declare no conflict of interest.

## References

1. Elasser, A.; Chow, T.P. Silicon carbide benefits and advantages for power electronics circuits and systems. *Proc. IEEE* **2022**, *90*, 969–986. [[CrossRef](#)]
2. Kimoto, T.; Watanabe, H. Defect engineering in SiC technology for high-voltage power devices. *Appl. Phys. Express* **2020**, *13*, 120101. [[CrossRef](#)]
3. Han, D.; Noppakunkajorn, J.; Sarlioglu, B. Comprehensive Efficiency, Weight, and Volume Comparison of SiC- and Si-Based Bidirectional DC–DC Converters for Hybrid Electric Vehicles. *IEEE Trans. Veh. Technol.* **2014**, *63*, 3001–3010. [[CrossRef](#)]
4. Umegami, H.; Harada, T.; Nakahara, K. Performance Comparison of Si IGBT and SiC MOSFET Power Module Driving IPMSM or IM under WLTC. *World Electr. Veh. J.* **2023**, *14*, 112. [[CrossRef](#)]
5. Shi, B.; Ramones, A.I.; Liu, Y.; Wang, H.; Li, Y.; Pischinger, S.; Andert, J. A review of silicon carbide MOSFETs in electrified vehicles: Application, challenges, and future development. *IET Power Electron.* **2023**, *16*, 2103–2120. [[CrossRef](#)]
6. Chung, G.Y.; Tin, C.C.; Williams, J.R.; McDonald, K.; Chanana, R.K.; Weller, R.A.; Pantelides, S.T.; Feldman, L.C.; Holland, O.W.; Das, M.K.; et al. Improved inversion channel mobility for 4H-SiC MOSFETs following high temperature anneals in nitric oxide. *IEEE Electron Device Lett.* **2001**, *22*, 176–178. [[CrossRef](#)]
7. Dhar, S.; Wang, S.R.; Ahyi, A.C.; Isaacs-Smith, T.; Pantelides, S.T.; Williams, J.R.; Feldman, L.C. Nitrogen and hydrogen induced trap passivation at the SiO<sub>2</sub>/4H-SiC interface. *Mater. Sci. Forum* **2006**, *527–529*, 949–954. [[CrossRef](#)]
8. Tachiki, K.; Mikami, K.; Ito, K. Mobility enhancement in heavily doped 4H-SiC (0001), (11–20), and (1–100) MOSFETs via an oxidation-minimizing process. *Appl. Phys. Express* **2022**, *15*, 071001. [[CrossRef](#)]
9. Cooper, J.A.; Melloch, M.R.; Singh, R.; Agarwal, A.; Palmour, J.W. Status and prospects for SiC power MOSFETs. *IEEE Trans. Electron Devices* **2002**, *49*, 658–664. [[CrossRef](#)]
10. Nakamura, T.; Nakano, Y.; Aketa, M.; Nakamura, R.; Mitani, S.; Sakairi, H.; Yokotsuji, Y. High performance SiC trench devices with ultra-low ron. In Proceedings of the 2011 International Electron Devices Meeting, Washington, DC, USA, 5–7 December 2011.
11. Shiomi, H.; Kitai, H.; Tamaso, H.; Fukuda, K. Development of a novel 1200-V-class 4H-SiC implantation-and-epitaxial trench MOSFET with low on-resistance. *Jpn. J. Appl. Phys.* **2016**, *55*, 04ER06. [[CrossRef](#)]
12. Peters, D.; Siemieniec, R.; Aichinger, T.; Basler, T.; Esteve, R.; Bergner, W.; Kueck, D. Performance and ruggedness of 1200V SiC—Trench—MOSFET. In Proceedings of the 29th International Symposium on Power Semiconductor Devices and IC's (ISPSD), Sapporo, Japan, 28 May–1 June 2017.
13. Sugawara, K.; Fukui, Y.; Tanaka, R.; Adachi, K.; Kagawa, Y.; Tomohisa, S.; Miura, N.; Suekawa, E.; Terasaki, Y. A Novel Trench SiC-MOSFETs Fabricated by Multiple-Ion-Implantation into Tilted Trench Side Walls (MIT2-MOS). In Proceedings of the International Exhibition and Conference for Power Electronics, Intelligent Motion, Renewable Energy and Energy Management, Online, 3–7 May 2021.
14. Shimizu, H.; Suto, T.; Miki, H.; Mori, Y.; Hisamoto, D.; Shima, A.; Kinoshita, K.; Murata, T.; Oda, T. Proposal of Vertical-channel FiN-SiC MOSFET toward Future Device Scaling. In Proceedings of the 35th International Symposium on Power Semiconductor Devices and IC's (ISPSD), Hong Kong, China, 28 May–1 June 2023.
15. Kagawa, Y.; Fujiwara, N.; Sugawara, K.; Tanaka, R.; Fukui, Y.; Yamamoto, Y.; Miura, N.; Imaizumi, M.; Nakata, S.; Yamakawa, S. 4H-SiC Trench MOSFET with Bottom Oxide Protection. *Mater. Sci. Forum* **2014**, *778–780*, 919–922. [[CrossRef](#)]
16. Wei, J.; Zhang, M.; Jiang, H.; Wang, H.; Chen, K.J. Dynamic Degradation in SiC Trench MOSFET With a Floating p-Shield Revealed With Numerical Simulations. *IEEE Trans. Electron Devices* **2017**, *64*, 2592–2598. [[CrossRef](#)]
17. Tanaka, R.; Kagawa, Y.; Fujiwara, N.; Sugawara, K.; Fukui, Y.; Miura, N.; Imaizumi, M.; Yamakawa, S. Impact of Grounding the Bottom Oxide Protection Layer on the Short-Circuit Ruggedness of 4H-SiC Trench MOSFETs. In Proceedings of the 26th International Symposium on Power Semiconductor Devices and IC's (ISPSD), Waikoloa, HI, USA, 15–19 June 2014.
18. Nanen, Y.; Kato, M.; Suda, J.; Kimoto, T. Effects of Nitridation on 4H-SiC MOSFETs Fabricated on Various Crystal Faces. *IEEE Trans. Electron Devices* **2013**, *60*, 1260–1262. [[CrossRef](#)]
19. Nakazawa, S.; Okuda, T.; Suda, J.; Nakamura, T.; Kimoto, T. Interface Properties of 4H-SiC (1120) and (1100) MOS Structures Annealed in NO. *IEEE Trans. Electron Devices* **2015**, *62*, 309–315. [[CrossRef](#)]

20. Caughey, D.M.; Thomas, R.E. Carrier mobilities in silicon empirically related to doping and field. *Proc. IEEE* **1967**, *55*, 2192–2193. [[CrossRef](#)]
21. Selberherr, S. *Analysis and Simulation of Semiconductor Devices*; Springer Science & Business Media: Dordrecht, The Netherlands, 1984.
22. Konstantinov, A.O.; Wahab, Q.; Nordell, N. Ionization rates and critical fields in 4H silicon carbide. *Appl. Phys. Lett.* **1997**, *71*, 90–92. [[CrossRef](#)]
23. Ren, N.; Wang, J.; Sheng, K. Design and Experimental Study of 4H-SiC Trenched Junction Barrier Schottky Diodes. *IEEE Trans. Electron Devices* **2014**, *61*, 2459–2465. [[CrossRef](#)]
24. Xu, H.; Ren, N.; Zhu, Z.; Wu, J.; Liu, L.; Guo, Q.; Sheng, K. Methodology for Enhanced Surge Robustness of 1.2-kV SiC MOSFET Body Diode. *IEEE Trans. Emerg. Sel. Topics Power Electron* **2020**, *10*, 5039–5047. [[CrossRef](#)]
25. Zhong, X.; Wang, B.; Sheng, K. Design and experimental demonstration of 1.35 kV SiC super junction Schottky diode. In Proceedings of the 28th International Symposium on Power Semiconductor Devices and IC's (ISPSD), Prague, Czech Republic, 12–16 June 2016.
26. Wang, C.; Wang, H.; Wang, B.; Cheng, H.; Sheng, K. Characterization and Analysis of 4H-SiC Super Junction JFETs Fabricated by Sidewall Implantation. *IEEE Trans. Electron Devices* **2022**, *69*, 2543–2551. [[CrossRef](#)]
27. Yu, L.C.; Dunne, G.T.; Matocha, K.S.; Cheung, K.P.; Suehle, J.S.; Sheng, K. Reliability Issues of SiC MOSFETs: A Technology for High-Temperature Environments. *IEEE Trans. Device Mater. Reliab.* **2010**, *10*, 418–426. [[CrossRef](#)]
28. Zhu, S.; Shi, L.; Jin, M.; Qian, J.; Bhattacharya, M.; Maddi, H.L.R.; White, M.H.; Agarwal, A.K.; Liu, T.; Shimbori, A.; et al. Reliability Comparison of Commercial Planar and Trench 4H-SiC Power MOSFETs. In Proceedings of the 2023 IEEE International Reliability Physics Symposium (IRPS), Monterey, CA, USA, 26–30 March 2023.
29. Matocha, K.; Dunne, G.; Soloviev, S.; Beaupre, R. Time-Dependent Dielectric Breakdown of 4H-SiC MOS Capacitors and DMOSFETs. *IEEE Trans. Electron Devices* **2008**, *55*, 1830–1834. [[CrossRef](#)]
30. Liu, T.; Zhu, S.; White, M.H.; Salemi, A.; Sheridan, D.; Agarwal, A.K. Time-Dependent Dielectric Breakdown of Commercial 1.2 kV 4H-SiC Power MOSFETs. *IEEE J. Electron Devices Soc.* **2021**, *9*, 633–639. [[CrossRef](#)]
31. Huang, X.; Wang, G.; Li, Y.; Huang, A.Q.; Baliga, B.J. Short circuit capability of 1200V SiC MOSFET and JFET for fault protection. In Proceedings of the 2013 Twenty-Eighth Annual IEEE Applied Power Electronics Conference and Exposition (APEC), Long Beach, CA, USA, 17–21 March 2013.
32. Lin, C.; Ren, N.; Xu, H.; Sheng, K. Performance and Short circuit Reliability of SiC MOSFETs With Enhanced JFET Doping Design. *IEEE Trans. Electron Devices* **2023**, *70*, 2395–2402. [[CrossRef](#)]
33. Lin, C.; Ren, N.; Xu, H.; Liu, L.; Zhu, Z.; Sheng, K. 1.2-kV Planar SiC MOSFETs With Improved Short circuit Capability by Adding Plasma Spreading Layer. *IEEE Trans. Electron Devices* **2023**, *70*, 4730–4736. [[CrossRef](#)]
34. Zhang, M.; Wei, J.; Jiang, H.; Chen, K.J.; Cheng, C.H. A New SiC Trench MOSFET Structure With Protruded P-Base for Low Oxide Field and Enhanced Switching Performance. *IEEE Trans. Device Mater. Reliab.* **2017**, *17*, 432–437. [[CrossRef](#)]
35. Kim, D.; DeBoer, S.; Jang, S.Y.; Morgan, A.J.; Sung, W. Improved Blocking and Switching Characteristics of Split-Gate 1.2 kV 4H-SiC MOSFET with a Deep P-well. In Proceedings of the 35th International Symposium on Power Semiconductor Devices and IC's (ISPSD), Hong Kong, China, 28 May–1 June 2023.
36. Kim, D.; DeBoer, S.; Mancini, S.A.; Isukapati, S.B.; Lynch, J.; Yun, N.; Morgan, A.J.; Jang, S.Y.; Sung, W. Static, Dynamic, and Short circuit Characteristics of Split-Gate 1.2 kV 4H-SiC MOSFETs. In Proceedings of the 2023 IEEE International Reliability Physics Symposium (IRPS), Monterey, CA, USA, 26–30 March 2023.

**Disclaimer/Publisher's Note:** The statements, opinions and data contained in all publications are solely those of the individual author(s) and contributor(s) and not of MDPI and/or the editor(s). MDPI and/or the editor(s) disclaim responsibility for any injury to people or property resulting from any ideas, methods, instructions or products referred to in the content.